E. RUNGE[1],✉
C. LIENAU[2]

Interpretation of near-field images
of semiconductor nanostructures

[1] Technische Universität Ilmenau, Fakultät für Mathematik und Naturwissenschaften and
Institut für Mikro- und Nanotechnologien, 98684 Ilmenau, Germany
[2] Max-Born-Institut für Nichtlineare Optik und Kurzzeitspektroskopie, Max-Born-Straße 2A,
12489 Berlin, Germany

ABSTRACT We discuss near-field wave function imaging, introducing a model for high spatial resolution photoluminescence imaging of semiconductor nanostructures. The model is applied to optically bright and dark exciton and biexciton states in different quantum dot systems, explicitly taking the experimental imaging configuration into account. Our results show that direct imaging of the exciton density is only possible in collection mode experiments with nonresonant excitation in the high-resolution limit. For other geometries and for biexcitonic states, the images reflect not only the size and shape of the wave function and the spatial resolution of the near-field probe but also in particular the inherent optical nonlinearity of the imaging process. Different examples for the effects of this nonlinearity are discussed, providing new insight into the interpretation of existing experiments, and guidelines for designing novel experiments.

PACS 78.67-n; 71.35.-y; 07.79.Fc

1   Introduction

Ever since the early days of near-field spectroscopy [1], near-field imaging and spectroscopy of low-dimensional semiconductor nanostructures, i.e., of quantum wells, wires and dots, has received considerable attention [2–14]. Substantial experimental progress has been achieved since then, and it is now possible to study the optical excitations of individual semiconductor quantum dots (QD) and quantum wires (QWR) with high spatial, spectral and temporal resolution. Coherent optical manipulation of individual quantum systems, specifically quantum dots, is just emerging and a rapidly developing novel field [9, 12, 13, 15–19]. For semiconductors, the study of individual quantum systems is particularly relevant, as – even with the most advanced growth techniques – fluctuations in size, geometry and/or composition of the nanostructures or their environment result in considerable variations of the optical spectra from one nanostructure to the next. Macroscopic far-field optical studies often probe densely packed and inhomogeneously broadened ensembles of nanostructures, giving only limited information about their microscopic optical properties.

On the theoretical side, ultrahigh spatial resolution spectroscopy of semiconductor nanostructures, with a resolution approaching or surpassing the spatial extent of the electronic wave functions, has sparked particular interest. Such high-resolution spectra are expected to be qualitatively different from conventional far-field optical spectra, because of, e.g., the non-local nature of the excitation and detection process [20, 21], different polarization selection rules [22], the loss of evanescent wave components in the far-field [23, 24] near-field coupling to optically dark states and a possible modification of their radiative decay [25].

Recent progress in apertureless near-field spectroscopy [26] and in the fabrication of aperture-based near-field fiber probes [27] has pushed the spatial resolution in near-field spectroscopy to less than 20 nm, reaching the spatial extent of electronic wave functions in semiconductor nanostructures. Such progress made it possible to attempt real-space imaging of individual quantum dots [11]. The photoluminescence (PL) of single excitons (X) and biexcitons (XX) localized in interface thickness fluctuations (interface quantum dots, IQD) of a thin GaAs quantum well (QW) were imaged with a resolution of about 30 nm. This is well below the apparent size of the measured X (100 nm) and XX (70 nm) PL images. Consequently, it was concluded that the extent of the biexcitonic center-of-mass wave function in these IQD is smaller than that of a single exciton.

In [11], the wave function imaging experiments were analyzed using a theoretical model assuming infinitely high resolution, and a full non-local description with finite resolution was given in [28, 29]. In [29], we have studied in particular the effect of the experimental configuration on the near-field images and shown that due to the inherent optical nonlinearity in exciton and biexciton spectroscopy as well as in the near-field imaging process, the near-field images represent a rather complicated convolution of the true local wave function probability density and the local electric field. Thus considerable care – and possibly a detailed theoretical analysis – is needed for a quantitative interpreting experimental near-field images in this high-spatial resolution regime.

It is the aim of this paper to describe in detail our theoretical approach used to simulate near-field wave function images and to extend this approach to the study of optically dark

✉ Fax: +49 +3677 69 3271, E-mail: Erich.Runge@TU-Ilmenau.DE

excitonic states, inaccessible by far-field studies. Again, special emphasis is put on studying the effect of the experimental imaging configuration to quantitatively predict the quite substantial influence of the near-field fiber probe on such images. We trust that this discussion is helpful in advancing near-field wave function imaging.

The article is structured as follows. In Sect. 2 we describe our theoretical model for simulating high-spatial resolution near-field imaging of semiconductor nanostructures. In Sect. 3, we discuss numerical results for imaging of optically bright and dark excitonic and biexcitonic states in spatially weakly confined (e.g., interface) quantum dots. In Sect. 4 these results are compared to studies of spatially strongly confined (e.g., Stranski–Krastanov) quantum dots. Analytical results helpful in comparing images obtained in different experimental configurations are given in Sect. 5. Some conclusions are presented in Sect. 6.

2   Theoretical model for near-field imaging of semiconductor nanostructures

The elementary optical excitations of semiconductor nanostructures are excitons, pairs of a quantum-confined electron in the conduction band and a hole in the valence band, bound by the Coulomb interaction. Exciton generation and luminescence are determined by the absorption rates r_α and inverse radiative lifetime τ_α^{-1} of the individual exciton states α, respectively. Up to constant prefactors, which shall be omitted below, both rates are given by the square of the transition amplitudes

$$\mathcal{M} = \langle \Psi_f | H_{\text{light–matt}} | \Psi_i \rangle \tag{1}$$

of the fundamental light–matter interaction Hamiltonian $H_{\text{light–matt}} \sim \int d\vec{r}\, c_c^\dagger(\vec{r}) c_v(\vec{r}) (e\vec{r}) \cdot \vec{E}(\vec{r} - \vec{R}_{\text{T}}, t)$. This expression describes that the generation/annihilation amplitude of a pair of an electron in the conduction band (c) and a hole in the valence band (v) at the position $\vec{r}$ is proportional to the dipole operator $e\vec{r}$ times the local photon field $\vec{E}$ [29–32]. We limit ourselves to monochromatic excitation, so that the latter is given by a time-dependent factor $e^{-i\omega t}$ and a factor $\vec{\mathcal{E}}(\vec{r} - \vec{R}_{\text{T}})$ describing its polarization and spatial distribution, which is centered around the NSOM tip position $\vec{R}_{\text{T}}$. For exciton transitions, $|\Psi_i\rangle$ and $|\Psi_f\rangle$ are the exciton state $|X\rangle$ and the empty crystal $|0\rangle$, respectively. For biexciton transitions, $|\Psi_i\rangle$ and $|\Psi_f\rangle$ are the biexciton $|XX\rangle$ and an exciton state $|X\rangle$, respectively.

For semiconductor nanostructures, the quantum confinement in at least one spatial direction is so strong that the carrier motion is confined to a few nm thick plane within the semiconductor. We use boldface letters for in-plane vectors, e.g., $\vec{r} = (\mathbf{r}, z)$. Because of the strong carrier confinement to essentially a plane with constant z, we can effectively drop the z dependence of the electric field, i.e., $\vec{\mathcal{E}}(\vec{r} - \vec{R}_{\text{T}}) = \vec{\mathcal{E}}(\mathbf{r} - \mathbf{R}_{\text{T}}, z) \equiv \vec{\mathcal{E}}(\mathbf{r} - \mathbf{R}_{\text{T}})$. Furthermore, we will assume that in-plane disorder is weak enough to allow excitons to move as entities. Formally, this corresponds to a factorization of the exciton wave function [33, 34]

$$\Psi_\alpha(\vec{r}_e, \vec{r}_h) \approx \psi_\alpha(\mathbf{R})\, \varphi(\mathbf{r}_e - \mathbf{r}_h)\, u_e(z_e) u_h(z_h) \tag{2}$$

or, in a slightly more general form,

$$\Psi_\alpha(\vec{r}_e, \vec{r}_h) \approx \psi_\alpha(\mathbf{R}) \varphi(\mathbf{r}_e - \mathbf{r}_h, z_e, z_h) \tag{3}$$

with a wave function $\varphi(\mathbf{r}_e - \mathbf{r}_h) u_e(z_e) u_h(z_h)$ or $\varphi(\mathbf{r}_e - \mathbf{r}_h, z_e, z_h)$ for the relative motion and the confinement of electron and hole in z direction, which is the same for all quantum states. The center-of-mass (COM) wave function $\psi_\alpha(\mathbf{R})$, on the other hand, varies from eigenstate to eigenstate. Only within an effective-mass one-band model is the COM coordinate given as $\mathbf{R} = (m_e \mathbf{r}_e + m_h \mathbf{r}_h)/(m_e + m_h)$. Nevertheless, this factorization into a fixed relative wave function and a state-dependent COM wave function is a good approximation under far more general conditions [35, 36].

The extent of the relative wave function is of the order of the exciton Bohr radius, i.e., typically a few nanometers. We make the realistic assumption that this is sufficiently smaller than the characteristic length of the electromagnetic field (i.e., the tip size) and the extension of the COM wave function within the nanostructure. This allows us to factor out the integrations over $\mathbf{r}_e - \mathbf{r}_h$, z_e, and z_h in (1) and to put the resulting prefactors together with Kane's matrix element and other prefactors into constants C in the expression

$$\mathcal{M}_{\text{X},\alpha} \equiv \mathcal{M}_{\text{X},\alpha}(\mathbf{R}_{\text{T}}) = C_{\text{X}}^{\text{IQD}} \int d\mathbf{R}\, \mathcal{E}(\mathbf{R} - \mathbf{R}_{\text{T}}) \psi_\alpha(\mathbf{R}) . \tag{4}$$

This so-called optical matrix element plays a central role in the theory of optical spectra of disordered quantum structures [32, 33, 37]. The far-field limit is obtained for constant $\mathcal{E}$ or for plane-wave-like fields as $\mathcal{M}_\alpha \sim \int d\mathbf{R}\, \psi_\alpha(\mathbf{R})$ or $\mathcal{M}_\alpha \sim \int d\mathbf{R}\, e^{i\mathbf{k} \cdot \mathbf{R}} \psi_\alpha(\mathbf{R})$.

In the following, we are mainly interested in describing luminescence experiments. This implies that we can neglect effects of coherent excitonic polarizations and interpret the results in terms of absorption and emission rates and probabilities of finding an exciton in a specific quantum state α. This is of course no longer justified in proposals to measure amplitude and phase of the exciton wave function by interferometric near-field techniques [38] and related experimental work [8] or in time-dependent coherent nonlinear near-field spectroscopy [9, 12, 13].

In general, we want to be able to describe experiments with both, resonant excitation of a specific quantum state α and detection of re-emitted light from this state, as well as with non-resonant excitation of (an ensemble of) quantum state(s) β at different energy and luminescence detection from state α. This requires in principle to account for the complex and strongly temperature-dependent energy redistribution processes within the nanostructure. To this end, we denote by $N_{\alpha\beta}$ the temperature-dependent probability that an exciton generated in the eigenstate β with energy ε_β decays radiatively from state α with energy ε_α (either resonant $\alpha = \beta$ or non-resonant $\alpha \neq \beta$).

Finally, we need to account for the experimental geometry of the near-field study. As usual, we distinguish between illumination-collection (i-c) mode, collection (c) mode and illumination (i) mode experiments. In the i-c-mode, both excitation and detection are performed through the near-field probe. In the c-mode, optical excitation is provided by conventional far-field light whereas the luminescence signal is

detected with a near-field probe. In the i-mode, the sample is locally excited in the near-field and the luminescence is detected in the far-field.

Typical near-field experiments involve non-resonant excitation and, mostly, real-space transfer of an exciton or electron–hole pair from the initial state β to α [3], accompanied with a relaxation in energy space, from ε_β to ε_α (mostly $< \varepsilon_\beta$). We start our discussion with a general expression for the near-field image. The incoherent excitonic luminescence I_X collected at frequency $\hbar\omega_c$ after illumination with excitation intensity I^{ex} at frequency ω_i recorded as function of tip position $\boldsymbol{R}_T$ is

$$I_X(\boldsymbol{R}_T, \hbar\omega_c) \sim \int d\omega_i \sum_{\alpha\beta} \delta(\hbar\omega_c - \varepsilon_\alpha)|\mathcal{M}_\alpha(\boldsymbol{R}_T)|^2$$
$$\times N_{\alpha\beta}|\mathcal{M}_\beta(\boldsymbol{R}_T)|^2 \delta(\hbar\omega_i - \varepsilon_\beta) I^{ex}(\hbar\omega_i) . \quad (5)$$

It involves a sum over all initial states β and all final states α at the corresponding energies (enforced by the delta functions) weighted with the rates r_β and τ_α^{-1} and for absorption and luminescence, respectively. The innocuously looking probability $N_{\alpha\beta}$ is in the general the most difficult part in this expression because it comprises the full non-equilibrium relaxation kinetics of a disordered quantum system [33]. Note that not only the quantum mechanical wave function ψ is different in $\mathcal{M}_\alpha$ and $\mathcal{M}_\beta$ but also the electric field $\mathcal{E}$. In collection mode, only $\mathcal{E}_\alpha$ is spatially localized.

Fortunately, with spatially weakly resolved far-field excitation, spectrally sufficiently broad to excite an ensemble of excitonic states, $I^{ex}(\hbar\omega_i)$, (5) simplifies to

$$I_X^c(\boldsymbol{R}_T, \hbar\omega_c) \sim \sum_\alpha \delta(\hbar\omega_c - \varepsilon_\alpha)|\mathcal{M}_\alpha(\boldsymbol{R}_T)|^2 . \quad (6)$$

For the last step, we used that in such experimental set-ups $\int d\omega_i \sum_\beta N_{\alpha\beta}|\mathcal{M}_\beta(\boldsymbol{R}_T)|^2 \delta(\hbar\omega_i - \varepsilon_\beta) I^{ex}(\hbar\omega_i)$ is expected to act as a spatially and spectrally unspecific supply of excitons.

In contrast, in typical resonant experiments ($\omega_i = \omega_c$), the diagonal terms $\alpha = \beta$ will dominate in (5). In particular in illumination-collection mode experiments, non-diagonal terms $\alpha \neq \beta$ can generally safely be neglected because the probability to find two different states at approximately the same energy ($\alpha \neq \beta$, but $\varepsilon_\alpha \approx \varepsilon_\beta$) is strongly suppressed by quantum mechanical level repulsion, see, e.g., [7, 39, 40]. Thus

$$I_X^{i-c}(\boldsymbol{R}_T, \hbar\omega_c) \sim \sum_\alpha \delta(\hbar\omega_c - \varepsilon_\alpha)|\mathcal{M}_\alpha(\boldsymbol{R}_T)|^4 . \quad (7)$$

The expressions (6) and (7) for the two practically relevant cases describe two opposite limits of the general expression (5). It is instructive to rewrite these in terms of exciton Green's functions

$$G(\boldsymbol{R}, \boldsymbol{R}'; E) = \sum_\alpha \frac{\psi_\alpha^*(\boldsymbol{R})\psi_\alpha(\boldsymbol{R}')}{E + i0 - \varepsilon_\alpha} \quad (8)$$

and density–density correlators

$$G^{(2)}(\boldsymbol{R}, \boldsymbol{R}'; E) = \sum_\alpha \frac{|\psi_\alpha(\boldsymbol{R})|^2 |\psi_\alpha(\boldsymbol{R}')|^2}{E + i0 - \varepsilon_\alpha} , \quad (9)$$

respectively. The intensity maps are convolutions of the form

$$I_X^c(\boldsymbol{R}_T, \hbar\omega_c)$$
$$\sim \Im \iint d\boldsymbol{R} d\boldsymbol{R}' \mathcal{E}(\boldsymbol{R} - \boldsymbol{R}_T) G(\boldsymbol{R}, \boldsymbol{R}'; \hbar\omega_c) \mathcal{E}(\boldsymbol{R}' - \boldsymbol{R}_T) .$$
$$(10)$$

In the corresponding equation for I_X^{i-c}, G should be replaced by $G^{(2)}$. Expressions equivalent to (10) have been derived by different groups and have, e.g., been used in [23, 24] in a discussion of the difference of spatially averaged local spectra and far-field spectra. They show very explicitly that the near-field response is a highly non-local optical process [20, 28].

In the following, we will use these expressions for simulating near-field optical images for specific experimental geometries and different types of semiconductor quantum dots.

3 Numerical results: Interface quantum dots

An important quantum dot model system is provided by thin semiconductor quantum wells of few nm thickness. In such quantum wells, local monolayer thickness fluctuations at the interfaces (interface roughness) and fluctuations of the alloy composition (alloy disorder) are unavoidable and result in a disordered potential for the exciton motion. This disordered potential leads to localization of excitons in local potential minima with a confinement energy of typically several meV. From a theoretical point of view these minima may be viewed as optimum fluctuations within an Anderson model with short-range disorder [41] and can be modeled by parabolic (harmonic oscillator HO) potentials. Because of the smoothness of hetero interfaces in high-quality samples, experimentalists often prefer to talk about growth islands and "natural" interface quantum dots (IQD) [42].

In this section, we discuss near-field imaging of bright and dark single exciton as well as biexciton states in interface quantum dots. These images are modeled based on the expressions (6) and (7) for the two different confinement potentials of a parabolic potential (HO) and a cylindrical box (box) [29]. Both allow for an easy analytical treatment in terms of exponential functions and Bessel functions. The respective ground states are written as

$$\psi_{gs}^{(HO)}(\boldsymbol{R}) \sim \exp(-R^2/5.544\ell_F^2) \quad (11)$$

and

$$\psi_{gs}^{(box)}(\boldsymbol{R}) \sim J_0(2.253 R/\ell_F) . \quad (12)$$

The full width at half maximum ℓ_F of the exciton density $|\psi|^2$ is related to the characteristic lengths ℓ_0 of the oscillator and the extension ℓ_{box} of the box via $\ell_f = \ell_0/1.665$ and $\ell_f = \ell_{box}/1.068$, respectively. The electromagnetic field distribution used in this simulation is described below.

3.1 Electromagnetic field distribution

We model the near-field fiber probe by a circular aperture of radius a_0 in a thin, perfectly conducting metal film placed a_0 right above the semiconductor sample [43]. The semiconductor is characterized by its optical density n

($n \simeq 3.5$ for GaAs). This is essentially the Bethe–Bouwkamp model [44, 45] of a circular metallic aperture illuminated with a plane wave polarized along the x axis. The incident electromagnetic field is characterized by its vacuum wave number k_0, or in dimensionless units by $k_0 a_0 \ll 1$. Bouwkamp [46] solved the model analytically based on Bethe's seminal paper [47]. The resulting field distribution close to the interface ($|z|/a_0 = 0.05$) is illustrated in Fig. 1 for the strong transverse component $\mathcal{E}_y$ und the longitudinal component $\mathcal{E}_z$. Both show pronounced features much narrower than a_0. These reflect singular contributions to the field-induced currents in the metal [44, 45]. Moving a few tens of nanometers further into the semiconductor, these features are rapidly smeared out and the transverse field components are close to an elliptical field profile polarized parallel to the incident field. At the same time, the profile becomes more and more isotropic. This transition from a highly anisotropic to an isotropic field distribution is illustrated in Fig. 2.

We characterize the depth dependence of the transverse electromagnetic field profile by its second moments

$$\alpha_{x,y}^2(z) = \iint dx\, dy \begin{Bmatrix} x^2 \\ y^2 \end{Bmatrix} \left(\mathcal{E}_x^2(x, y, z) + \mathcal{E}_y^2(x, y, z) \right) \quad (13)$$

FIGURE 2 Electromagnetic field in a semiconductor medium with $n = 3.5$ below a circular aperture with radius a_0 incident radiation with $k_0 a_0 = 0.02$. *Circle* and *dots*: mean-square width, (13), of field distribution in x and y direction, respectively. *Diamonds*: anisotropy parameter. *Triangles*: field intensity

along the principal axes, its anisotropy $(\alpha_x - \alpha_y)/(\alpha_x + \alpha_y)$, and its strength. The decay of the field divergencies occurs on distances $z < 0.1 a_0$. For distances larger than about a_0/n, the field distributions start to diverge, resulting in a reduction of the field anisotropy and a substantial loss in spatial resolution with increasing depth of the nanostructure layer.

In our simulations, the longitudinal field components are neglected, since they are reduced by a factor of $1/n^2$ ($n \simeq 3.5$ for GaAs) at the air/semiconductor interface and because heavy-hole excitons in quantum wells have only in-plane dipole moments [33]. This is different for light hole transitions, which may therefore be enhanced in near-field experiments [22]. Convincing experimental evidence for a strong near-field effect on the polarization selection rules is, however, to our knowledge still lacking. Note the sign change of $\mathcal{E}_z$ (lower panel of Fig. 1), which may lead to cancellations in the matrix elements.

3.2 Near-field images of optically bright and dark exciton states

Near-field images for ground state excitons in a cylindrical box of 107 nm radius ($\ell_F = 100$ nm) calculated for a collection and illumination-collection geometry are shown in Fig. 3. An aperture radius of $a_0 = 10$ nm is assumed and the quantum dot is placed 20 nm below the sample surface. The circular symmetry of the excitonic wave function is approximately reproduced in all cases. Only the collection mode image match the probability density of the excitonic wave function. In this case, the image in Fig. 3a is close to that obtained in the limit infinitely high NSOM resolution. Here, the field distribution $\mathcal{E}(R - R_T)$ can be replaced by a δ function. The collection-mode image is $I_X^c(R_T, \varepsilon_\alpha) \sim |\mathcal{M}_{X,\alpha}(R_T)|^2 \sim |\psi_\alpha(R_T)|^2$, which is the exciton density. In the illumination-collection mode, however, the squared exciton density is imaged, $I_X^{i-c}(R_T, \epsilon_\alpha) \sim |\psi_\alpha(R_T)|^4$.
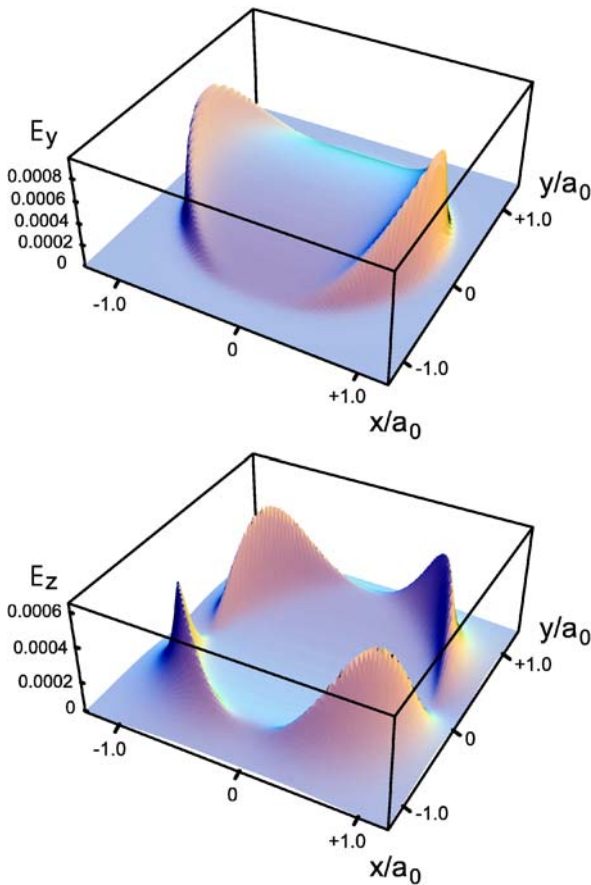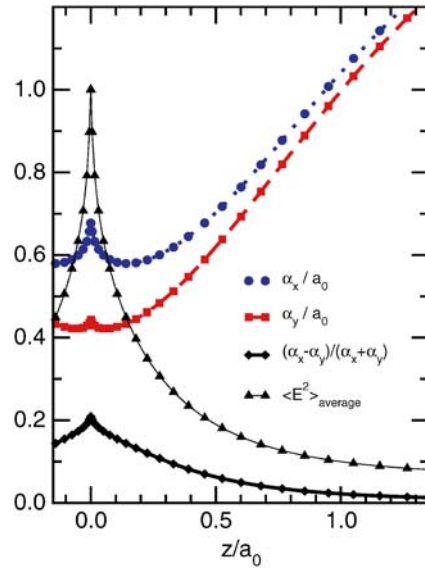

FIGURE 1 Illustration of field anisotropy: Electric field in y direction (*upper panel*) and z direction at distance $z = 0.05 a_0$ from metallic aperture. Calculated in Bethe–Bouwkamp theory for $k_0 a_0 = 0.02$ and linear incident polarization along the x axis. Note the $\mathcal{E}_z$ vanishes along the y axis, where it changes its sign
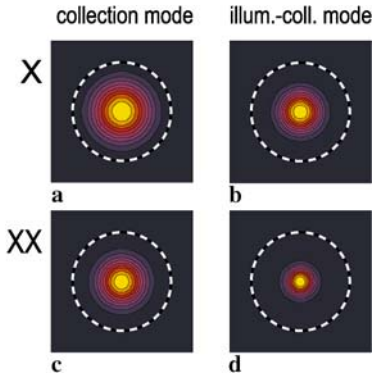
FIGURE 3 Calculated near-field images of excitons (*top row*) and biexcitons (*bottom row*) of an interface quantum dot in GaAs 20 nm below the sample surface for a collection mode (*left column*) and illumination-collection mode (*right column*) geometry. The FWHM width of the exciton density is $\ell_F = 100$ nm, the aperture radius is $a_0 = 10$ nm. The cylindrical box potential with a radius of 107 nm is indicated by a *dashed line*. Intensities are color-coded in linear 10% steps. Smaller images are found for the illumination-collection mode geometry and for biexcitonic transitions due to the non-linear nature of the corresponding imaging process

FIGURE 4 Calculated collection-mode near-field images of excitons in cylindrical boxes with 107 nm (*upper row*, $\ell_F = 100$ nm) and 32 nm (*lower row*, $\ell_F = 30$ nm) radius. Aperture radii are 10 nm and 80 nm, respectively. From left to right: $\psi_{gs}^{(box)}$, $\psi_{1,y}^{(box)}$, and $\psi_{1x}^{(box)}$. The incident light is linearly polarized along the vertical y axis. The intensities are normalized and color-coded in linear 10% steps. Normalization factors relative to the ground state panel (*left*) in each row are included in exponential notation. Note that all exciton densities strictly vanish outside the boxes marked by the *dashed circles*

This corresponding reduction in image size results solely from the nonlinearity of the imaging process, and does not reflect a change in size of the quantum-mechanical wave function.

We now turn to collection-mode near-field imaging of optically dark states. As an example, we consider the two degenerate first excited states in a circular box, which both do not couple to far-field radiation. Their wave functions are $\psi_{1,x}^{(HO)}(\boldsymbol{R}) \sim R \cos\phi_R \psi_{gs}^{(HO)}(\boldsymbol{R})$ and $\psi_{1,y}^{(HO)}(\boldsymbol{R}) \sim R \sin\phi_R \psi_{gs}^{(HO)}(\boldsymbol{R})$ for the parabolic potential as well as $\psi_{1,x}^{(box)}(\boldsymbol{R}) \sim \cos\phi_R J_1(3.590 R/\ell_F)$ and $\psi_{1,y}^{(box)}(\boldsymbol{R}) \sim \sin\phi_R J_1 (3.590 R/\ell_F)$ for the cylindrical box. Obviously, the optical matrix element (4) vanish if $\mathcal{E}$ is sufficiently slowly varying, because the contributions from the positive and negative lobes in the angular ϕ_R integrations cancel each other.

In the limit that the aperture diameter is considerably smaller than the extent of the exciton COM wave function [Fig. 4b,c], the collection-mode near-field images indeed match the excitonic density closely. The images of $\psi_{1,x}$ and $\psi_{1,y}$ are rotated by 90°, but otherwise almost identical. Their total intensity is considerably smaller than for the bright ground state.

More interesting, and probably more realistic, is the case that the aperture is larger, and of similar dimension as the exciton wave function, see lower row of Fig. 4. Now, the image of the round (*s*-like) ground state exciton is strongly deformed by the anisotropic electromagnetic field distribution [29]. Here, the aperture can be moved along the y axis by almost the distance a_0 away from the exciton, still picking up some intensity from the anisotropic field distribution. This effect is strongly enhanced for the first excited states $\psi_{1,x}$ and $\psi_{1,y}$. As long as the exciton is close to the center of the aperture, the field gradient is small and the image appears dark because positive and negative contributions to the optical matrix element (4) tend to cancel each other. Noticeable intensity is obtained when only one lobe (either positive or negative) overlaps with the electromagnetic field distribution. Correspondingly, the apparent images of the excited states $\psi_{1,x}$ and
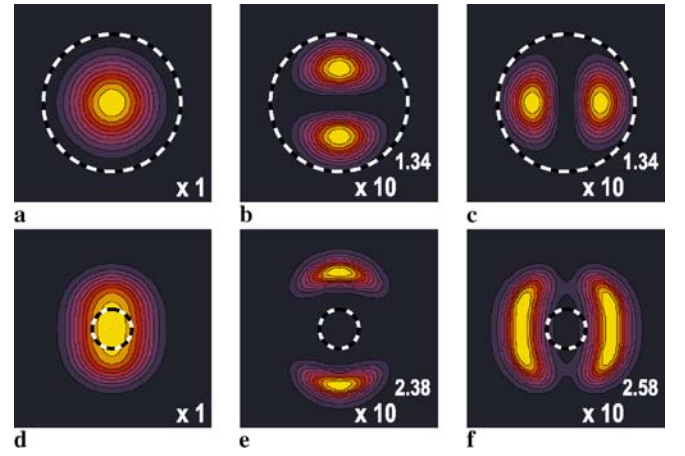
$\psi_{1,y}$ are localized almost exclusively outside of the potential well (dashed circle in the figure), whereas the excitons themselves are exclusively inside the well. With Fig. 1 in mind, it is easy to see why the maps of $\psi_{1,x}$ and $\psi_{1,y}$ differ so much and why the latter leads to a larger overall extension, but to narrower features. The figure includes the normalization factors. These range from ≈ 20 for Fig. 4b,c to ≈ 400 for Fig. 4f. This pronounced reduction in image intensity indicates that while dark mode imaging appears in general feasible even if the spatial resolution is only of the order of the exciton wave function [28], it becomes quite challenging because of the strong reduction of image intensity with decreasing resolution. We emphasize that the potential well in Fig. 4 was chosen to be round and that the x–y differences are therefore solely due to the anisotropic field. At the same time, we warn that round potential wells are highly unrealistic. Experimentally, this is empirically known from, e.g., scanning tunneling microscope images or polarization anisotropies of natural interface quantum dots [42]. It is less known, however, that such "round" minima are highly unlikely in a statistical optimum fluctuation scenario as well. Therefore, this is explicitly shown in the appendix.

3.3   *Biexciton non-linearities*

Simultaneously with the first near-field images of excitonic wave functions, images of biexciton states were reported in [11]. A striking feature was that the apparent size of the biexciton image, e.g., 70 nm, was considerably smaller than that of the corresponding exciton image, e.g., 100 nm. This raises the interesting question to what extent the inherent nonlinearity and non-locality involved in the near-field imaging process (5) affects such correlated excitonic states. Again, a factorization into a COM part ψ_{XX} depending on the biexciton in-plane position $\boldsymbol{R}_{XX}$ and a relative part φ_{XX} is a good starting point for a theoretical discussion [29, 48]

$$\Psi_{XX}^{IQD}(\vec{r}_{e1}, \vec{r}_{e2}, \vec{r}_{h1}, \vec{r}_{h2}) \approx \psi_{XX}(\boldsymbol{R}_{XX})$$
$$\times \varphi_{XX}(\boldsymbol{r}_{e1} - \boldsymbol{r}_{hh}, \boldsymbol{r}_{e2} - \boldsymbol{r}_{hh}, \boldsymbol{r}_{h1} - \boldsymbol{r}_{h2}, z_{e1}, z_{e2}, z_{h1}, z_{h2}) . \tag{14}$$

We use a representation in terms of the hole COM $\boldsymbol{r}_{hh} = (\boldsymbol{r}_{h1} + \boldsymbol{r}_{h2})/2$, ignore for simplicity spin degrees of freedom, and assume that the antisymmetry required by the Pauli principle is provided by the spin wave function. This is the case for the lowest optically active biexciton state. While the limits of the factorization approximation have not yet been analyzed in great detail for biexcitons, it is expected to be a good approximation for weak disorder and/or large IQD. Accurate relative wave functions φ_{XX} calculated by Riva et al. [49] confirm that the average e–e and h–h separations are of the order of a_B, i.e., comparable to typical e–h distances. The total extent of φ_{XX} is less than about $2a_B$ even for XX binding energies of only $\simeq 0.2$ meV. Given that XX binding energies of 1–3 meV are typically found [18, 50] in IQD in thin QWs, the actual extent of φ_{XX} is expected to be even smaller [48].

Inserting the factorized forms for the bixeciton (14) and exciton (3) wave functions into the optical transition matrix element (1) yields

$$\mathcal{M}_{XX,\alpha} \equiv \mathcal{M}_{XX,\alpha}(\boldsymbol{R}_T)$$
$$= C_{XX}^{IQD} \int d\boldsymbol{R} \psi_{X,\alpha}(\boldsymbol{R}) \mathcal{E}(\boldsymbol{R} - \boldsymbol{R}_T, z) \psi_{XX,\alpha}(\boldsymbol{R}) . \tag{15}$$

In principle, this matrix element should have indices referring to the final biexciton state and indices referring to the initial exciton state. However, we consider here for simplicity the simplest case of a biexciton which can be thought of as consisting of two excitons with the same quantum numbers α (except for spin). Thus, α may refer to, e.g., the lowest state in a local energy minimum at a specific real-space position. Again, the optical matrix element (15) in the limit of spatially constant or plane-wave-like fields $\mathcal{E}$ is a central ingredient for the theory of biexciton far-field spectra of disordered QW and QWR samples.

Analogously to the derivation of the exciton images in collection mode with non-resonant excitation and illumination-collection mode with resonant excitation, one finds

$$I_{XX}^{i-c}(\boldsymbol{R}_T) = |\mathcal{M}_{XX}(\boldsymbol{R}_T)|^4 |\mathcal{M}_X(\boldsymbol{R}_T)|^2 \tag{16}$$
$$I_{XX}^{c}(\boldsymbol{R}_T) = |\mathcal{M}_{XX}(\boldsymbol{R}_T)|^2 . \tag{17}$$

Note that the generation probability in the i–c-mode is proportional to the square of the local intensity, because the exciton has to be generated before the biexciton transition can be observed [50]. This nonlinear intensity dependence gives rise to important differences in the spatial variation of exciton and biexciton PL images [29]. This is easily seen for the limit of arbitrarily good resolution. The resulting "images" reflect neither the exciton nor the biexciton density, but certain products:

$$I_{XX}^{i-c}(\boldsymbol{R}_T) \xrightarrow{\mathcal{E} \to \delta(\boldsymbol{R} - \boldsymbol{R}_T)} \text{const} |\psi_{X,\alpha}(\boldsymbol{R}_T)|^6 |\psi_{XX,\alpha}(\boldsymbol{R}_T)|^4$$
$$I_{XX}^{c}(\boldsymbol{R}_T) \longrightarrow \text{const} |\psi_{X,\alpha}(\boldsymbol{R}_T)|^2 |\psi_{XX,\alpha}(\boldsymbol{R}_T)|^2 .$$

For specific illustrations, we consider again parabolic potentials and box potentials. The biexciton ground-state COM

wave functions expressed in terms of their excitonic counter parts are

$$\psi_{gs,XX}^{(HO)}(\boldsymbol{R}) = \sqrt{2} \psi_{gs}^{(HO)}(\boldsymbol{R}\sqrt{2}) \tag{18}$$
$$\psi_{gs,XX}^{(box)}(\boldsymbol{R}) = \psi_{gs}^{(box)}(\boldsymbol{R}) . \tag{19}$$

The $\sqrt{2}$ factors for the harmonic potential result from the smaller kinetic energy of the heavier biexciton and the stronger confinement (twice as many particles) [29]. For the comparison in Fig. 3, we consider the box confinement, where the X and XX COM wave functions are identical. Thus, the obvious differences between panels (a) and (c), as well as panels (b) and (d) result solely from the non-linearities in the imaging process, which – in a lax notation – can be summarized as $I_X^c : I_X^{i-c} : I_{XX}^c : I_{XX}^{i-c} \sim \psi^2 : \psi^4 : \psi^4 : \psi_\alpha^{10}$. Note that in this case not even the collection mode image in the limit of infinitely high resolution reflects the XX wave function or its density.

4   Images of small, strongly confining quantum dots

The factorization (3) of the exciton wave function in a COM part and a relative wave function obviously breaks down for electron–hole pairs confined to quantum dots with size comparable to the Bohr radius or below, i.e., $\lesssim 10$ nm. Typical examples are colloidal QD and, in particular, self-organized dots resulting from Stranski–Krastanov growth [51]. As noted very early by Banyai [52], the kinetic energy contribution of the exciton's constituents grows with the squared inverse dot diameter, whereas the attractive Coulomb energy grows linearly. Thus in the limit of very strong localization, the kinetic energy dominates and electron and hole can be treated as independent entities. The corresponding factorization

$$\Psi_0^{SQD}(\boldsymbol{r}_e, \boldsymbol{r}_h) \sim \phi_{gs}(\boldsymbol{r}_e) \phi_{gs}(\boldsymbol{r}_h) \tag{20}$$

with the same confinement function (but different confinement energies) for electron and hole give for the optical matrix element ($\boldsymbol{r}_e = \boldsymbol{r}_h$)

$$\mathcal{M}_{eh}^{SQD}(\boldsymbol{R}_T) = \int d\boldsymbol{r} \mathcal{E}(\boldsymbol{r} - \boldsymbol{R}_T) \phi_{gs}^2(\boldsymbol{r}) . \tag{21}$$

We assumed for simplicity of notation that the confinement in z direction is so strong that we can neglect the corresponding degrees of freedom. Even the best near-field microscopes today have a resolution that is larger than the diameter of such small dots, in particular, considering that they are mostly buried below the sample surface. Thus, $\mathcal{E}$ varies slowly compared to ϕ_{gs}^2 and can be replaced by its value at the average dot position $\bar{\boldsymbol{r}}$. Consequently,

$$\mathcal{M}_{eh}^{SQD}(\boldsymbol{R}_T) \approx \mathcal{E}(\bar{\boldsymbol{r}} - \boldsymbol{R}_T) \tag{22}$$
$$I_{eh}^{c}(\boldsymbol{R}_T) \sim |\mathcal{E}(\bar{\boldsymbol{r}} - \boldsymbol{R}_T)|^2 \tag{23}$$
$$I_{eh}^{i-c}(\boldsymbol{R}_T) \sim |\mathcal{E}(\bar{\boldsymbol{r}} - \boldsymbol{R}_T)|^4 . \tag{24}$$

Near-field images of such small dots are thus essentially mapping a specific vector component of the electric field distribution of the near-field probe.

For completeness, we mention that for 2e–2h states (corresponding to biexcitons) in small strongly confining dots the ground state wave function is expected to approximately factorize in four single-particle factors

$$\Psi_{XX}^{SQD} \approx \phi_{gs}(\vec{r}_{e1})\phi_{gs}(\vec{r}_{e2})\phi_{gs}(\vec{r}_{h1})\phi_{gs}(\vec{r}_{h2}) \,. \tag{25}$$

The resulting "biexciton" transition matrix element coincides with the exciton transition matrix element, because the second e-h pair is (approximately) independent from the first one

$$\mathcal{M}_{2e\text{-}2h}^{SQD}(\boldsymbol{R}_T) \sim \mathcal{M}_{eh}^{SQD}(\boldsymbol{R}_T) \sim \mathcal{E}(\overline{\boldsymbol{r}} - \boldsymbol{R}_T) \,. \tag{26}$$

In analogy to (16) and (17), the intrinsic non-linearity of biexcitonic absorption, i.e., the fact that excitons have to be created first, leads to

$$I_{2e\text{-}2h}^{c}(\boldsymbol{R}_T) = |\mathcal{M}_{XX}(\boldsymbol{R}_T)|^2 \sim |\mathcal{E}(\overline{\boldsymbol{r}} - \boldsymbol{R}_T)|^2 \sim I_{eh}^{c}(\boldsymbol{R}_T) \tag{27}$$

$$I_{2e\text{-}2h}^{i\text{-}c}(\boldsymbol{R}_T) = |\mathcal{M}_{2e\text{-}2h}(\boldsymbol{R}_T)|^4 |\mathcal{M}_{eh}(\boldsymbol{R}_T)|^2 \sim |\mathcal{E}(\overline{\boldsymbol{r}} - \boldsymbol{R}_T)|^6 \,. \tag{28}$$

5   Analytical results

The model in Sect. 3.1 showed that, not too close to the near-field probe, the electrical in-plane field can approximately be described by an anisotropic Gaussian profile [$\boldsymbol{R} = (X, Y)$]

$$\mathcal{E}(\boldsymbol{R}) \sim e^{-X^2/2\alpha_x^2} e^{-Y^2/2\alpha_y^2} \,. \tag{29}$$

Assuming Gaussian wave functions for exciton, $\sim e^{-R^2/2\ell_0^2}$, and biexciton, $\sim e^{-R^2/\ell_0^2}$, i.e., for parabolic potential minima, one finds again Gaussian profiles for the optical matrix elements

$$\mathcal{M}_X(\boldsymbol{R}_T) \sim e^{-\dfrac{X_T^2}{2\ell_0^2}\dfrac{1}{1+\tilde{\alpha}_x^2} - \dfrac{y_T^2}{2\ell_0^2}\dfrac{1}{1+\tilde{\alpha}_y^2}} \tag{30}$$

$$\mathcal{M}_{XX}(\boldsymbol{R}_T) \sim e^{-\dfrac{X_T^2}{2\ell_0^2}\dfrac{3}{1+3\tilde{\alpha}_x^2} - \dfrac{y_T^2}{2\ell_0^2}\dfrac{3}{1+3\tilde{\alpha}_y^2}} \tag{31}$$

with the abbreviation $\tilde{\alpha}_{x,y} = \alpha_{x,y}/\ell_0$. As products of Gaussians, the spatial images $I(\boldsymbol{R}_T)$ are all given by an anisotropic Gaussian function. Their widths $\sigma_{x,y}$ are directly taken from (5), (7), (16), and (17) as

$$\left(\frac{\sigma_X^c}{\ell_0}\right)^2 : \left(\frac{\sigma_X^{i\text{-}c}}{\ell_0}\right)^2 : \left(\frac{\sigma_{XX}^c}{\ell_0}\right)^2 : \left(\frac{\sigma_{XX}^{i\text{-}c}}{\ell_0}\right)^2 \tag{32}$$

$$= \left(\frac{2}{1+\tilde{\alpha}^2}\right)^{-1} : \left(\frac{4}{1+\tilde{\alpha}^2}\right)^{-1} : \left(\frac{2\times 3}{1+3\tilde{\alpha}^2}\right)^{-1} :$$

$$\left(\frac{4\times 3}{1+3\tilde{\alpha}^2} + \frac{2}{1+\tilde{\alpha}^2}\right)^{-1}$$

$$= \frac{1+\tilde{\alpha}^2}{2} : \frac{1+\tilde{\alpha}^2}{4} : \frac{1+3\tilde{\alpha}^2}{6} : \frac{1+4\tilde{\alpha}^2+3\tilde{\alpha}^4}{14+18\tilde{\alpha}^2} \,.$$

We omit x, y indices. In the limit of infinitely high resolution $\tilde{\alpha} \to 0$:

$$\sigma_X^c : \sigma_X^{i\text{-}c} : \sigma_{XX}^c : \sigma_{XX}^{i\text{-}c} : \ell_0 = 0.71 : 0.50 : 0.41 : 0.27 : 1 \,. \tag{33}$$

The results of [11] give roughly 100 nm:70 nm = 1.4 and are thus not too far off this simple estimate $\sigma_X^c : \sigma_{XX}^c = 0.71 : 0.41 = 1.7$.

The width of the images of small, strongly confining dots, (23), (24), (27), and (28), are related to each other by fixed ratios [29]

$$\sigma_{eh}^c : \sigma_{eh}^{i\text{-}c} : \sigma_{2e\text{-}2h}^c : \sigma_{2e\text{-}2h}^{i\text{-}c} : \alpha = \frac{1}{\sqrt{2}} : \frac{1}{2} : \frac{1}{\sqrt{2}} : \frac{1}{\sqrt{6}} : 1 \,. \tag{34}$$

6   Conclusions

In summary, we have introduced a theoretical model for high spatial resolution incoherent near-field photoluminescence imaging of semiconductor nanostructures. The model is applied to optically bright and dark exciton and biexciton states in different quantum dot systems, explicitly taking the experimental imaging configuration into account. Perhaps the most general conclusion that can be drawn from our simulations is that direct imaging of the local exciton density happens only in collection mode experiments with non-resonant excitation in the high-resolution limit. For other geometries and for biexcitonic states, the images reflect not only the size and shape of the wave function and the spatial resolution of near-field probe but also, in particular, the inherent optical nonlinearity of the imaging process. If the optical resolution surpasses the size of the wave function structures, the imaging nonlinearity mainly results in variations in size of the near-field images in different configurations, whereas the symmetry of the image reflects that of the excitonic wave function. If the resolution is comparable to the wave function size, this no longer holds. The images may reflect the characteristic field divergences of metallic aperture probes if the nanostructure is placed very close to the fiber probe or, more typical for buried semiconductor nanostructures, the inherent anisotropy of the electric field distribution at distances of few tens of nanometers between probe and object. The rather complex convolution of true local wave function probability density, local electric field and imaging nonlocality and nonlinearity calls for a careful theoretical analysis of near-field wave function experiments. It is the intention of this article to contribute to such a discussion. For a full quantitative analysis of experimental results it might be interesting and necessary to go beyond the simplified model outlined. Radiative couplings between near-field probe and quantum object and the effects of carrier dynamics, quantum coherences and quantum transport on the imaging process are interesting topics that yet remain to be explored from both a theoretical as well as experimental perspective.

Appendix: Geometry of deep minima

To a good approximation, excitons in quantum strutures with growth-related disorder can often be described as point-like quantum particles in a random energy "landscape"

$v(\mathbf{r})$ [53, 54]. The landscape is characterized by the strength of the energy fluctuations $\sigma^2 = \overline{v^2}$ and the shape of the potential-potential correlations $\overline{v(\mathbf{r})v(\mathbf{r}')}/\sigma^2$. The latter determines a parameter

$$a = \frac{\overline{v_{xy}^2 v^2}}{\overline{v_x^2}^2} \geq \frac{1}{2} \qquad (A.1)$$

which takes the value of $a = 1$ for Gaussian correlations. The probability to find a minimum at energy $v_{\min}$ with the second derivatives (curvatures) $v_{\pm}$ is [with $\sigma \equiv 1$ for ease of notation] [55, 56]

$$\mathcal{P}(v_{\min}, v_+, v_-) =$$

$$\frac{v_+ - v_-}{\sqrt{2\pi a}} e^{-\frac{1}{8a}(v_+ + v_-)^2} \frac{e^{-\frac{1}{2}v_{\min}^2}}{\sqrt{2\pi}} \frac{e^{-\frac{1}{2(2a-1)}\left(\frac{v_+ + v_-}{2} - v_{\min}\right)^2}}{\sqrt{2\pi(2a-1)}} . \qquad (A.2)$$

One finds that even deep in the tail at $v_{\min} = 3\sigma$ the minima are quite anisotropic, with $(v_+ - v_-)/(v_+ + v_-)$ being of the order of 20% [33]. The corresponding exciton wave functions will be equally anisotropic (anisotropic harmonic oscillator potential). This suggests that, whenever isotropic images wave function images are recorded for IQD, this should thus be taken as indication that the resolution is insufficient to resolve the wave function.

REFERENCES

1 H.F. Hess, E. Betzig, T.D. Harris, L.N. Pfeiffer, K.W. West, Science **264**, 1740 (1994)
2 J. Levy, V. Nikitin, J.M. Kikkawa, A. Cohen, N. Samarth, R. Garcia, D.D. Awschalom, Phys. Rev. Lett. **76**, 1948 (1996)
3 A. Richter, G. Behme, M. Süptitz, C. Lienau, T. Elsaesser, M. Ramsteiner, R. Nötzel, K.H. Ploog, Phys. Rev. Lett. **79**, 2145 (1997)
4 G. Eytan, Y. Yayon, M. Rappaport, H. Shtrikman, I. Bar-Joseph, Phys. Rev. Lett. **81**, 1666 (1998)
5 Y. Toda, O. Moriwaki, M. Nishioka, Y. Arakawa, Phys. Rev. Lett. **82**, 4114 (1999)
6 A.M. Mintairov, T.H. Kosel, J.L. Merz, P.A. Blagnov, A.S. Vlasov, V.M. Ustinov, R.E. Cook, Phys. Rev. Lett. **87**, 277 401 (2001)
7 F. Intonti, V. Emiliani, C. Lienau, T. Elsaesser, V. Savona, E. Runge, R. Zimmermann, R. Nötzel, K.H. Ploog, Phys. Rev. Lett. **87**, 076 801 (2001)
8 J.R. Guest, T.H. Stievater, G. Chen, E.A. Tabak, B.G. Orr, D.G. Steel, D. Gammon, D.S. Katzer, Science **293**, 2224 (2001)
9 T. Guenther, C. Lienau, T. Elsaesser, M. Glanemann, V.M. Axt, T. Kuhn, S. Eshlaghi, A.D. Wieck, Phys. Rev. Lett. **89**, 057 401 (2002)
10 Y. Yayon, A. Esser, M. Rappaport, V. Umansky, H. Shtrikman, I. Bar-Joseph, Phys. Rev. Lett. **89**, 157 402 (2002)
11 K. Matsuda, T. Saiki, S. Nomura, M. Mihara, Y. Aoyagi, S. Nair, T. Takagahara, Phys. Rev. Lett. **91**, 177 401 (2003)
12 T. Unold, K. Mueller, C. Lienau, T. Elsaesser, A.D. Wieck, Phys. Rev. Lett. **92**, 157 401 (2004)
13 T. Unold, K. Mueller, C. Lienau, T. Elsaesser, A.D. Wieck, Phys. Rev. Lett. **94**, 137 404 (2005)
14 A. Feltrin, F. Michelini, J.L. Staehli, B. Deveaud, V. Savona, J. Toquant, X.L. Wang, M. Ogura, Phys. Rev. Lett. **95**, 177 404 (2005)
15 T.H. Stievater, X. Li, D.G. Steel, D. Gammon, D.S. Katzer, D. Park, C. Piermarocchi, L.J. Sham, Phys. Rev. Lett. **87**, 133 603 (2001)
16 H. Kamada, H. Gotoh, J. Temmyo, T. Takagahara, H. Ando, Phys. Rev. Lett. **87**, 246 401 (2001)
17 A. Zrenner, E. Beham, S. Stufler, F. Findeis, M. Bichler, G. Abstreiter, Nature **418**, 612 (2002)
18 X.Q. Li, Y.W. Wu, D. Steel, D. Gammon, T.H. Stievater, D.S. Katzer, D. Park, C. Piermarocchi, L.J. Sham, Science **301**, 809 (2003)
19 B. Patton, U. Woggon, W. Langbein, Phys. Rev. Lett. **95**, 266 401 (2005)
20 O. Mauritz, G. Goldoni, F. Rossi, E. Molinari, Phys. Rev. Lett. **82**, 847 (1999)
21 C. Simserides, U. Hohenester, G. Goldoni, E. Molinari, Phys. Rev. B **62**, 13 657 (2000)
22 G.W. Bryant, Appl. Phys. Lett. **72**, 768 (1998)
23 G. Pistone, S. Savasta, O. Di Stefano, R. Girlanda, Phys. Rev. B **67**, 153 305 (2003)
24 G. Pistone, S. Savasta, O. Di Stefano, R. Girlanda, Appl. Phys. Lett. **84**, 2971 (2004)
25 U. Hohenester, G. Goldoni, E. Molinari, Phys. Rev. Lett. **95**, 216 802 (2005)
26 A. Hartschuh, E.J. Sanchez, X.S. Xie, L. Novotny, Phys. Rev. Lett. **90**, 095 503 (2003)
27 K. Matsuda, T. Saiki, S. Nomura, M. Mihara, Y. Aoyagi, Appl. Phys. Lett. **81**, 2291 (2002)
28 U. Hohenester, G. Goldoni, E. Molinari, Appl. Phys. Lett. **84**, 3963 (2004)
29 E. Runge, C. Lienau, Phys. Rev. B **71**, 035 347 (2005)
30 H. Haug, S.W. Koch, *Quantum Theory of the Optical and Electronic Properties of Semiconductors* (World Scientific, Singapore, 1990)
31 L.C. Andreani, F. Bassani, F. Tassone, In: *Optics of Excitons in Confined Systems*, ed. by A. D'Andrea, R. Del Sole, R. Girlanda, A. Quattropani, IOP Conference Series Number 123 (IOP Press, Bristol, 1992), p. 25
32 R. Zimmermann, E. Runge, V. Savona, In: *Quantum Coherence, Correlation and Decoherence in Semiconductor Nanostructures*, ed. by T. Takagahara (Elsevier Science, Oxford, 2003), p. 89–165
33 E. Runge, *Solid State Physics*, Vol. 57, ed. by H. Ehrenreich, F. Spaepen (Academic Press, San Diego, 2002) p. 149–305 and references therein
34 R. Zimmermann, F. Große, E. Runge, Pure Appl. Chem. **69**, 1179 (1997)
35 A. Siarkos, E. Runge, R. Zimmermann, Phys. Rev. B **61**, 10 854 (2000)
36 A. Siarkos, E. Runge, Phys. Rev. B **61**, 16 854 (2000)
37 V. Savona, In: *Electron and Photon Confinement in Semiconductor Nanostructures*, ed. by B. Deveaud, A. Quattropani, P. Schwendimann (IOP Press, Amsterdam, 2003) p. 219
38 O. Di Stefano, S. Savasta, G. Pistone, G. Martino, R. Girlanda, Phys. Rev. B **68**, 165 329 (2003)
39 G. von Freymann, E. Kurtz, C. Klingshirn, M. Wegener, Appl. Phys. Lett. **77**, 394 (2000)
40 J.R. Guest, T.H. Stievater, D.G. Steel, D. Gammon, D.S. Katzer, D. Park, In: Quantum Electronics and Laser Science Conference, OSA Technical Digest (Optical Soc. America, Washington, DC, 2000) p. 6
41 I.M. Lifshits, S.A. Gredeskul, L.A. Pastur, *Introduction to the Theory of Disordered Systems* (Wiley, New York, 1988)
42 D. Gammon, E.S. Snow, B.V. Shanabrook, D.S. Katzer, D. Park, Phys. Rev. **76**, 3005 (1996)
43 B. Hanewinkel, A. Knorr, P. Thomas, S.W. Koch, Phys. Rev. B **55**, 13 715 (1997)
44 R.D. Grober, T. Rutherford, T.D. Harris, Appl. Opt. **35**, 3488 (1996) and references therein
45 Y. Leviatan, J. Appl. Phys. **60**, 1577 (1986)
46 C.J. Bouwkamp, Philips Res. Rep. **5**, 321 (1950)
47 H.A. Bethe, Phys. Rev. **66**, 163 (1944)
48 O. Heller, P. Lelong, G. Bastard, Phys. Rev. B **56**, 4702 (1997)
49 C. Riva, F.M. Peeters, K. Varga, V.A. Schweigert, Phys. Stat. Solidi B **234**, 50 (2002)
50 K. Brunner, G. Abstreiter, G. Böhm, G. Tränkle, G. Weimann, Phys. Rev. Lett. **73**, 1138 (1994)
51 D. Bimberg, M. Grundmann, N.N. Ledentsov, *Quantum Dot Heterostructures* (John Wiley, New York, 1998)
52 L. Banyai, Phys. Rev. B **39**, 8022 (1989)
53 F. Yang, M. Wilkinson, E.J. Austin, K.P. O'Donnell, **70**, 323 (1993)
54 F. Yang, M. Wilkinson, E.J. Austin, K.P. O'Donnell, Phys. Rev. Lett. **72**, 1945 (1994)
55 H. Nickolaus, H.-J. Wünsche, F. Henneberger, Phys. Rev. Lett. **81**, 2586 (1998)
56 W. Langbein, R. Zimmermann, E. Runge, J.M. Hvam, Phys. Stat. Solidi B **221**, 349 (2000)